Journal of the Meteorological Society of Japan

EARLY ONLINE RELEASE

The DOI for this manuscript is
DOI:10.2151/jmsj.2025-011
J-STAGE Advance published date: January 14, 2025
The final manuscript after publication will replace the preliminary version at the above DOI once it is available.

Characteristics of raindrop size distribution using 10-year disdrometer data in eastern Japan

Takashi UNUMA, Hiroshi YAMAUCHI, Teruyuki KATO,

Akihito UMEHARA, Akihiro HASHIMOTO,

Meteorological Research Institute
Japan Meteorological Agency, Tsukuba, Ibaraki, Japan

Ahoro ADACHI,

Meteorological Collage
Japan Meteorological Agency, Kashiwa, Chiba, Japan

and

Nobuhiro NAGUMO

Atmosphere and Ocean Department
Japan Meteorological Agency, Minato, Tokyo, Japan

submitted to *Journal of the Meteorological Society of Japan*
June 4, 2024

Corresponding author: Takashi Unuma, Meteorological Research Institute, Japan Meteorological Agency, 1-1, Nagamine, Tsukuba, Ibaraki 305-0052 JAPAN
Email: unuma@mri-jma.go.jp
Tel: +81-29-853-8711

Abstract

The drop size distribution (DSD) of precipitation particles is a fundamental property for characterizing rainfall. This study statistically clarified the characteristics of DSDs using approximately 10 years of DSD data obtained from a ground-based optical disdrometer in Kumagaya, the eastern part of Japan. The results showed that DSDs tended to maintain their shape even as rainfall intensity (R) increased, and they tended to be distributed in a certain region, i.e., the mass-weighted mean diameter (D_m) ~2.0–3.0 mm and the generalized intercept parameter (N_w) ~2×10^3–3×10^4 mm^{-1} m^{-3}, of the DSD parameter space defined by D_m and N_w. The quasi-equilibrium shape of the DSDs, which is rarely observed only 16 cases in this study, was likely to be different characteristics between maritime and continental convection. Among them, the contribution to R was large when D_m or N_w was effectively increased with temporal change based on an error analysis. DSD characteristics were also identified by statistically evaluating the relationship between the specific differential phase (K_{DP}) and R in DSDs for C-band polarimetric weather radar. The results showed that the coefficient of the K_{DP}–R relation tended to be larger (>24.0) during the warm season (from May to October) and smaller (<21.0) during the cold season (from January to April and from November to December) when assuming a temperature of 10 degrees Celsius, whereas the exponent of the relation had no apparent trend. Furthermore, it is likely that the slope parameter, one of the DSD parameters, can be optimized for stronger rainfall events with a nearly same size distribution.

Keywords raindrop size distribution; heavy rainfall; K_{DP}–R relation

1. Introduction

The drop size distribution (DSD) of precipitation particles is a key property characterizing rainfall that has been studied worldwide in various ways, including by laboratory experiments, numerical modeling, and observational analyses. In cloud microphysical processes, the larger drops, once they grow to about 10 micrometers in radius by the condensation of water vapor, are produced by coalescence process before they reach the ground. The effects on raindrops of collisional coalescence and collisional breakup, which envisions to be obtained under warm rain processes, in particular have long been studied. The earlier studies showed that DSDs characteristically have shown to be trimodal (Valdez and Young 1985, Brown 1986, Feingold et al. 1988, Chen and Lamb 1994) based on Low and List (1982)'s parameterization and ground-based observations using impact type Joss-Waldvogel disdrometers, while laboratory experiments have shown them to be bimodal (Steiner and Waldvogel 1987; List et al. 1987; Asselin de Beauville et al. 1988). Subsequent studies showed that there were problems with the Joss-Waldvogel disdrometer showing a false peak mainly associated with uneven operation (Sheppard 1990) and this instrument-related peak was evaluated by McFarquhar and List (1993). McFarquhar (2004a) developed a more physical based parameterization of the fragment size distributions by colliding raindrops and showed that the stationary distribution obtained numerically was to be bimodal. More recently, Straub et al. (2010) also showed the bimodal stationary distribution obtained numerically using computational fluid dynamics program (Beheng et al. 2006; Schlottke et al. 2010). These studies suggest that laboratory-based and theoretical parameterizations for numerically representing an equilibrium distribution are approaching closure (McFarquhar 2010). Nevertheless, observational studies (McFarquhar et al. 1996; D'Adderio et al. 2018) showed that DSDs rarely reached an equilibrium shape except in heavy rainfall events (Garsia-Garcia and Gonzalez 2000). Such observational results were not always consistent with the numerically obtained stationary distributions, probably due to evaporation (Brown 1993; Hu and Srivastava 1995), size sorting by updrafts (Kollias et al. 2001; McFarquhar and List 1991), number of observational samples (McFarquhar 2004b), and wind shear (Dawson II et al. 2015).

Although there were the inconsistencies between numerically obtained stationary distributions and observed distributions as described above, a few studies tried to extract stationary distributions from observational DSDs and to examine their characteristics. Low and List (1982) identified a relationship dependent on raindrop size to parameterize the breakup efficiency in terms of collisional kinetic energy (CKE), and they showed that as a result of raindrop coalescence, inflection points occur in DSDs at raindrop diameters of around 1.0–2.6 mm. Thus, when collisional breakups occur, decreases in the frequency of raindrops with diameters around 1.5 mm and increases in the frequency of raindrops with diameters of less than 1 mm and with diameters of 2–3 mm often produce bimodal DSDs (McFarquhar 2004a; Prat and Barros 2007; McFarquhar 2010; Straub et al. 2010; D'Adderio et al. 2015) as stationary distributions, as shown in McFarquhar (2004a)'s Fig. 15 or Straub et al. (2010)'s Fig. 10. Based on this prior work, D'Adderio et al. (2015) have proposed an algorithm to detect DSDs that have approached equilibrium shape by taking into account this characteristic of the bimodal distribution that an inflection point occurs. Also, D'Adderio et al. (2018) found that DSDs were likely to have an inflection point, which were referred to as an equilibrium shape in their study, when the temporal changes of the rainfall intensity (R) were large. Their method finding an inflection point in a DSD could represent one of the characteristics of the bimodal stationary distribution obtained from the previous studies (e.g., McFarquhar 2004a; Straub et al. 2010); however, it is necessary not only to find an inflection point of a DSD, but also to quantitatively assess the degree of shape similarities in the size distribution.

An equilibrium shape of DSD, in addition to having a bimodal shape, is characterized by a large-drop tail slope with a slope parameter (Λ) of around 2 mm^{-1} of the DSD. This feature can be demonstrated by using an optical spectrometer (Willis and Tattelman 1989), and it has been identified in case studies that used optical disdrometers. Friedrich et al. (2013), who studied DSDs observed during storm passages in the United States, showed that the Λ of DSDs was constant during strong rainfall events, and Unuma et al. (2023) and Unuma (2024) have shown that in heavy rainfall systems in Japan, the value Λ was approaching to around 2 mm^{-1} as R increases. These results suggest that it might be possible to identify equilibrium shape of DSDs in terms of Λ (see Appendix A and Fig. A1).

From the DSD parameter perspectives, Bringi et al. (2003) have proposed that the DSDs observed during several field campaigns can be broadly classified into maritime and continental climatic regimes according to the DSD parameters (e.g., the mass-weighted mean diameter D_m and the generalized intercept parameter N_w). Dolan et al. (2018) have conducted an empirical orthogonal function (EOF) analysis of global observations, including observations in different climate regions, and have proposed a region-independent DSD regime that takes account of the relationship between the characteristics of DSDs in different regions and their dominant cloud microphysical processes. It has been pointed out that in the tropics, in particular, it may not be possible to simply separate precipitation processes below the melting layer into stratiform and convective rainfall regimes, which is considered to be an important characteristic of precipitation processes that produce heavy rainfall in the tropics. For example, Thompson et al. (2018) showed that the convective-stratiform separation is not effective for rainfall estimation when R is stronger. In Japan, however, no study has demonstrated the characteristic features of DSDs based on long-term ground-based observations.

Quantitative precipitation estimation (QPE) of warm-season heavy rainfall remains a challenging task (e.g., Fritsch and Carbone 2004). R estimation techniques are the cornerstone of short-term (i.e., typically less than one hour) forecasting, and various relational formulas for R estimation have been proposed that use ground-based measurements and/or polarimetric weather radar observations (e.g., Ryzhkov and Zrnić 2019; WMO 2024). Among them, a method using the specific differential phase (K_{DP}) for estimating R (Sachidananda and Zrnić 1987) is less susceptible to ground clutter and anomalous propagation (Zrnić and Ryzhkov 1996; Ryzhkov and Zrnić 1998) and has many advantages when used with C-band radar observations, which are less susceptible to rainfall attenuation. Many studies have proposed a K_{DP}–R relation for C-band polarimetric radar observations (May et al. 1999; Bringi et al. 2011; Vulpiani et al. 2012; Figueras et al. 2012; Wang et al. 2013; Thompson et al. 2018; Chen et al. 2017). The relation proposed for C-band radar observations in Japan (Bringi et al. 2006; Adachi et al. 2015) has been applied on a case study basis, but the relation has not been established by using long-term data, especially, ground-based DSD observation data.

In recent years, various aspects of specific rainfall events in Japan have been studied (e.g., Tsuguti and Kato 2014; Unuma and Takemi 2016, Kato 2020). Most of these studies identify a precipitating area where R or the accumulated rainfall amount exceeds a certain threshold as a heavy rainfall event; however, it has been pointed out that R or the accumulated rainfall amount are not sufficient to define heavy rainfall (Hirockawa et al. 2020; Unuma and Takemi 2021). In addition, because R is obtained by integrating a DSD, it should be possible to examine the precise characteristics of strong rainfall in terms of not only R itself but also DSD properties such as size distribution related parameters. For example, Adachi et al. (2013) and Otsubo and Adachi (2024) used the relationship between differential reflectivity (Z_{DR}) and R for the QPE on case study basis. However, Z_{DR} is affected by rainfall attenuation in C-band polarimetric weather radar, suggesting that the K_{DP}–R relation, which is less affected by rainfall attenuation, is reasonable to use for C-band radar. Furthermore, to use operational polarimetric weather radar to accurately detect high-impact weather events that cause heavy rainfall, it is necessary to clarify the appropriate relation between R and K_{DP}, which is expected to contain a signal that can be used for the detection of precursors of precipitating systems that may cause heavy rainfall-related disasters.

Therefore, the first purpose of this study is to statistically characterize DSDs of strong rainfall events observed in Kumagaya, eastern Japan, and the second purpose is to obtain an optimized K_{DP}–R relation for strong rainfall to improve QPE. In this paper, Section 2 presents details of the data and methodology, Section 3 presents the results, which are discussed in Section 4. In the final, conclusion section, some implications of this study are discussed.

2. Data and Methodology

The data used were obtained by a first-generation OTT-Parsivel disdrometer (Löffler-Mang and Joss 2000) installed at Kumagaya (Fig. 1). A Parsivel disdrometer measures the drop size and fall velocity of precipitation particles. The original data are observed within a laser beam sheet and output in 32 drop-size categories (i direction) and 32 fall-velocity categories (j direction). The laser beam sheet of the Parsivel disdrometer is 180 mm long, 30 mm wide, and 1 mm thick, and the effective sampling area S (m^{-2}) is expressed as 0.180 × (0.030 – L/2), where L is a size parameter that depends on the drop size. The drop

Fig. 1

diameters range from 0.2 to 25 mm and velocities range from 0.2 to 20 m s^{-1}, respectively. The two smallest drop size categories were not used in this study because of their low signal-to-noise ratios (Tokay et al. 2013). Observed drop sizes were converted into the equivalent volume diameter (D_e) in accordance with Adachi et al. (2013) (hereafter, D_e is represented simply as D). The drop-size distribution $N(D)$ (mm^{-1} m^{-3}) was then obtained as follows:

$$N(D) = \sum_{j=1}^{32} \frac{C_{i,j}}{S\, V_j(D_i)\, \Delta t\, \Delta D_i}, \quad (1)$$

where $C_{i,j}$ represents the raw output having a matrix structure with 32 drop-size categories and 32 fall-velocity categories, $V_j(D_i)$ (m s^{-1}) is the fall velocity for each drop size D_i, Δt is the observation time interval (60 s in this study), ΔD_i is the drop-size spread (mm) in equivalent volume diameters, and the subscripts i and j indicate the drop size and fall velocity category, respectively. To eliminate unreliable data, disdrometer observations with R less than 0.1 mm hr^{-1}, or a number of observed particles less than 10 drops per 1 min in $C_{i,j}$, was excluded following Tokay et al. (2014). We verified R data against a tipping-bucket-type rain gauge data. First, we assumed that the formula of Atlas et al. (1973) as described the fall velocity of raindrops and used data with fall velocities within ±50% of the formula values. After this quality control step, R (mm hr^{-1}) was calculated from the observed DSD data with the following equation:

$$R = 6 \times 10^{-4}\, \pi \sum_{i=1}^{32} \sum_{j=1}^{32} \frac{C_{i,j}}{S\, V_j(D_i)\, \Delta t \Delta D_i}\, V_j(D_i)\, D_i^3, \quad (2)$$

which is the mass flux, i.e., the mass of raindrops falling on a unit area per unit time.

Figure 2 shows a scatter plot of *R* calculated with Eq. (2) using DSDs observed by the Parsivel disdrometer versus those obtained by the rain gauge. The values generally fell along a straight one-to-one line (correlation coefficient 0.92; slope of the fitted line 0.95); this result indicated that the Parsivel disdrometer-related *R* were good agreement with rain gauge data. Fig. 2

The DSD parameters were calculated by assuming a normalized gamma distribution and calculated the parameter using the moment technique (Hardin and Guy 2017). The normalized gamma distribution of drop sizes (Testud et al. 2001) was expressed as

$$N(D) = N_w f(\mu)\left(\frac{D}{D_m}\right)^{\mu} \exp\left[-(4+\mu)\frac{D}{D_m}\right], \quad (3)$$

where the generalized intercept parameter N_{w} (mm^{-1} m^{-3}) was calculated as

$$N_{\mathrm{w}} = \frac{4^4\, LWC}{\pi \rho_{\mathrm{w}}\, D_{\mathrm{m}}^4}, \quad (4)$$

and $f(\mu)$ was defined as

$$f(\mu) = \frac{\Gamma(4)}{4^4}\,\frac{(4+\mu)^{(4+\mu)}}{\Gamma(4+\mu)}. \quad (5)$$

Here, μ is a shape parameter, ρ_{w} is the density of water (g m^{-3}), and Γ is the Gamma function. The liquid water content *LWC* (g m^{-3}) and the mass-weighted mean diameter D_{m} (mm) were obtained with following equations:

$$LWC = \frac{\pi \rho_w}{6}\sum_{i=1}^{32}\sum_{j=1}^{32}\frac{C_{i,j}}{S\, V_j(D_i)\,\Delta t \Delta D_i} D_i^3, \quad (6)$$

and

$$D_{\mathrm{m}} = \frac{\sum_{i=1}^{32}\sum_{j=1}^{32}\frac{C_{i,j}}{S\,V_j(D_i)\,\Delta t\Delta D_i}D_i^4}{\sum_{i=1}^{32}\sum_{j=1}^{32}\frac{C_{i,j}}{S\,V_j(D_i)\,\Delta t\Delta D_i}D_i^3}. \quad (7)$$

The exponential distribution of drop size was expressed as

$$N(D) = N_0\exp(-\Lambda D), \quad (8)$$

where N_0 (mm^{-1} m^{-3}) is the intercept parameter and Λ (mm^{-1}) is the slope parameter, which are calculated by the moment relation method of Zhang et al. (2008).

The analysis period was from 00:00 Japan Standard Time (JST: 9 hours ahead of Coordinated Universal Time) on 1 January 2010 to 23:59 JST on 31 December 2022. The data were output every 1 min. Several outages for instrument maintenance occurred during the analysis period; the actual number of available samples was 294,756.

To detect the equilibrium shape of DSDs, the algorithm of D'Adderio et al. (2015, 2018) was applied to Parsivel disdrometer data. The algorithm is based on the concept that a DSD that has an inflection point caused by a decrease in the frequency of raindrops with a diameter of around 1.5 mm, and an increase in the frequency of larger and smaller drops as a result of collisional coalescence and breakup. Briefly, the calculation procedure of D'Adderio et al. (2015) is as follows: Over 5 bins from smaller (i.e., 1.0 mm in their study and we used the same value in this study) to larger diameters, the linear best fit of the considered DSD obtained from Eq. (1) is calculated. Starting points are considered from 1.0 to 1.6 mm with 0.2-mm-diameter spreads, and then four linear relationships are calculated. The maximum slope among the four relationships is defined as the highest slope (HS; units,

mm^{-2} m^{-3}). The occurrence of an inflection point (i.e., HS > 0) in a DSD indicated that the DSD has approached equilibrium shape as one of their characteristics. Focusing on stronger rainfall events, only events with R equal to or greater than 10 mm hr^{-1} were applied (3,736 DSDs). In addition, considering the variety and diversity in the height of stationary distribution peaks, a DSD was extracted as one that can be explained by more than 90% of the stationary distribution obtained in McFarquhar (2004a) or Straub et al. (2010) for the stationary distribution normalized by its total number concentration. In procedure, coefficients of determination were calculated after satisfying the HS > 0 conditions of 261 DSDs. The DSDs for which the coefficients of determination between Parsivel's DSD and one of the stationary distributions was equal to or larger than 0.9 were collected. Finally, the total number of the obtained DSDs was 16; hereafter, the DSDs were called quasi-equilibrium DSDs (QEDSDs) in this study. A way of the quantifications for a similarity of the prescribed stationary distributions obtained from theoretical parameterization (Straub et al. 2010) or laboratory-based parameterization (McFarquhar 2004a) was applied to the procedure in addition to finding an inflection point in a DSD (e.g., D'Adderio et al. 2015). The additional procedure makes it possible to extract the QEDSD from observed DSDs even if a stationary distribution observed in nature may differ from the size distributions obtained from theoretical parameterization (Straub et al. 2010) or laboratory-based parameterization (McFarquhar 2004a) due to uncertainties of the peak heights in the measured DSD.

3. Results

At first, a general feature of the observed DSDs was described using the DSD parameters. Fig. 3

A scatter plot of the DSD parameters D_m and N_w in relation to R is shown in Fig. 3. When R was relatively weak (e.g., ~3 mm hr^{-1}), the variation of D_m and N_w were very large, ranging from 1.0 to 5.0 mm and from 10^1 to 10^5 mm^{-1} m^{-3}, respectively, whereas when R exceeded 50 mm hr^{-1}, the variation of D_m was relatively small (e.g., ~1.0–2.0 mm), and most cases were distributed within a specific region of the DSD parameter space, i.e., D_m ~2.0–3.0 mm and N_w ~2×10^3–3×10^4 mm^{-1} m^{-3}. The regions of the DSD parameter space corresponding to continental convection (solid line rectangle), maritime convection (dashed line rectangle), and stratiform rainfall (dotted line) types, as classified by Bringi et al. (2003), are also shown. R ranged from 10 to 80 mm hr^{-1} in the maritime convection region, and from 3 to 50 mm hr^{-1} in the continental convection region. Most cases with R exceeding 50 mm hr^{-1} were distributed between the maritime convection and the continental convection regions, whereas many cases with weak R (<5 mm hr^{-1}) corresponded to stratiform rainfall cases and could be clearly distinguished from convective cases. Most of QEDSD cases (cyan markers) were distributed between continental and maritime convection regions or in larger D_m (>2.5 mm) region. The characteristics of each marker will be described later.

To understand differences in the shape of QEDSDs, the frequency distributions of all data and QEDSD cases (Fig. 4) were examined. For QEDSD cases (Fig. 4b), the range from the 10^{th} to the 90^{th} percentile of DSDs in diameter from 0.5 to 1.0 mm was narrower compared Fig. 4

with that for all data (Fig. 4a). On the other hand, in diameter larger than 1.0 mm, the range from the 25th to the 75th percentile of DSDs as well as from the 10th to the 90th percentile is slightly wider than that for all data, which is probably due to the variability of the peak height (e.g., McFarquhar 2004a). Although there were some variations in QEDSDs, the shape of the distribution was significantly different among them; There are an inflection point between 1.0 mm and 2.0 mm in diameter and a secondary peak in QEDSDs with a relatively higher concentration for larger diameter (>2.0 mm). Additionally, the distribution of median values is quite similar to that of Straub et al. (2010), and the distribution of 25th percentile resembles that of McFarquhar (2004a).

To see how the quasi-equilibrium shape has been established, the diameter size which shows an inflection point in the distributions is examined (Fig. 5). The size ranges from 1.0 to 1.6 mm with the most frequent diameter of 1.59 mm, indicating that the shape of DSDs seems to be approaching an equilibrium shape although there are small variations in the inflection points of the distribution. Fig. 5

We next examined the contributions of temporal changes in D_m and N_w to changes in R in order to evaluate how R increases or decreases in terms of DSD parameters. Additionally, we applied error analysis (e.g., Bevington and Robinson 2003) to quantify the contribution of changes in D_m and N_w to changes in LWC. First, we transformed Eq. (4) to the following:

$$LWC = \frac{\pi \rho_w}{4^4} N_\mathrm{w} D_\mathrm{m}^4, \quad (9)$$

where $\frac{\pi \rho_w}{4^4}$ is a constant. Next, taking the logarithm of both sides of Eq. (9) and differentiating each side, we obtained the following equation:

$$\frac{\Delta LWC}{LWC} = \frac{\Delta N_\mathrm{w}}{N_\mathrm{w}} + 4\frac{\Delta D_\mathrm{m}}{D_\mathrm{m}}. \quad (10)$$

Here, Δ indicates the difference in parameter values between the time when HS > 0 and one minute before. Note that Eqs. (2) and (6) can be regarded as approximately proportional to the integral of the DSD multiplied by *D* to the 3rd moments; thus, the analysis in this study was performed on an assumption that the change in *R* was proportional to that in *LWC*. Here, we focused on QEDSD cases and applied the assumption to the analysis.

A scatter plot between the two terms on the right-hand side of Eq. (10) in relation to the change of *R* for QEDSDs is shown in Fig. 6. The QEDSD cases of increasing *R* were distributed in the first (star), second (square), and fourth (triangle) quadrants, whereas those cases of decreasing *R* were less likely to be located in the first quadrant. Comparison of the frequencies of cases among the quadrants indicated that the highest number of cases (8 DSDs) were those in which N_w increased and D_m decreased, followed by cases in which both N_w and D_m increased (4 DSDs), and those in which D_m increased but N_w decreased (3 DSDs). Note that in 3 DSDs among the highest number of cases rainfall amounts rapidly increased. Only 1 DSDs showed decreases in both N_w and D_m. Compared to Fig. 3, half of the second quadrant cases with increased N_w and decreased D_m were distributed to correspond to the cases with larger D_m (>3.0 mm) cases, which is mainly related to the wide range of frequency distributions in the shape of QEDSDs (Fig. 4b). The other half of second (D_m decreased and N_w increased) and most of the fourth (D_m increased and N_w decreased)

Fig. 6

quadrant cases were mostly distributed between maritime and continental convective areas except the first (both D_m and N_w increased).

When DSDs approach an equilibrium shape, Λ approaches a constant value (e.g., Willis and Tattelman 1989) as described in the introduction. Therefore, we investigated the relationship between R and Λ (Fig. 7). The DSDs displayed a typical shape such that for larger value of R, Λ values were concentrated ranging from 1.4 to 2.0 mm^{-1}; this trend was especially noticeable for stronger R (e.g., >10 mm hr^{-1}). In addition, the QEDSD cases (red crosses) were mainly distributed in the area with Λ < 2 mm^{-1}, which is consistent with the previous studies (e.g., Fredrich et al. 2013; Unuma 2024). Fig. 7

The K_{DP}–R relation used to estimate R in DSDs was also examined in the long-term disdrometer data because an optimal K_{DP}–R relation, which is less dependent on DSD (Sachidananda and Zrnić 1987) than the other relations, is expected to be obtained. The K_{DP}–R relation calculated was as follows:

$$R(K_{\mathrm{DP}}) = a\, K_{\mathrm{DP}}^{b}, \quad (11)$$

where coefficient a and exponent b are constant. The coefficients (Table 1) were estimated from ground-based DSD data at Kumagaya during each month, where K_{DP} was obtained from the Parsivel disdrometer data by the T-matrix method (Mishchenko et al. 1996) using a drop-shape relationship proposed by Beard and Chuang (1987), assuming the temperature of 10 degrees C, and the transmitting frequency of 5.4 GHz in the temporal interval of 1 min, and then R was obtained by Eq. (2). In general, the values of a and b at Table 1

Kumagaya are smaller than those shown previously (Yamauchi et al. 2012; Adachi et al. 2015). The value of *a* tends to be larger in the warm (e.g., from May to October) season and smaller in the cold (e.g., from January to April and from November to December) season (Table 1), whereas *b* shows a large monthly variation but no apparent trend.

4. Discussion

4.1 Quasi-Equilibrium DSD obtained in this study

QEDSDs which resemble numerically obtained stationary distribution are likely to occur in Japan. Previous studies have mainly discussed the equilibrium shape of DSD based on observations in tropical and mid-latitude regions (e.g., Zawadzki and De Agostinho Antonio 1988; McFarquhar et al. 1996; D'Adderio et al. 2018). Recently, it has been pointed out that the equilibrium shape of DSD can also be observed in subtropical regions for the R >15 mm hr^{-1} condition (Murata et al. 2020). In addition, equilibrium shape of DSD was observed in a very humid environment when heavy rainfall was brought in Japan (Misumi et al. 2021; Unuma et al. 2023; Unuma 2024). These observations and the characteristics obtained in this study suggest that equilibrium shape of DSD can also be observed in a warm and humid climate region such as Japan. Although the environmental variability (i.e., thermodynamic properties and/or vertical wind shear) may affect the DSD shape (e.g., Hu and Srivastava 1995; Kollias et al. 2001; McFarquhar and List 1991; Dawson II et al. 2015), such effects need to be investigated and are left for a future work.

The QEDSD characteristics of maritime and continental convection were distinct from those of stratiform rainfall, as has been shown previously (Bringi et al. 2003; Dolan et al. 2018), and QEDSD characteristics were likely to be differed somewhat between continental and maritime convection at least based on the results of the ground-based DSD observations. The frequencies of D_m and/or N_w to the increase in *LWC* (proportional to R) was higher than those of both D_m and N_w increased for the QEDSD cases (Fig. 6). It has been pointed out that the increasing N_w is the main contributor to increasing R mainly due to small variations of D_m in an equilibrium DSD in the tropics (e.g., Zawadzki and de Agostinho Antonio 1988), which is partly consistent with the results obtained in this study. The cases in which N_w increased and D_m decreased (8 DSDs) accounted for most frequent cases, followed by cases in which both N_w and D_m increased (4 DSDs), and cases in which D_m increased but N_w decreased (3 DSDs) among the QEDSDs as shown in Fig. 6.

In Japan, heavy rainfall events from organized precipitating systems often cause extensive damage (e.g., Tsuguti and Kato 2014; Unuma and Takemi 2016). As revealed in this study, in a series of such precipitating systems associated with heavy rainfall, the rainfall intensification, which depends on the increase of D_m and/or N_w, may contribute to warm-season heavy rainfall in Japan.

As shown in Fig. 3, QEDSD cases were not associated with the specific parameter space, i.e., stronger R with D_m ranging from 1.5 to 3.0 mm and $N_w > 3\times10^3$ mm^{-1} m^{-3}. Thus, the characteristics with the conditions of $R >= 40$ mm hr^{-1} and $\Lambda < 2$ mm^{-1} based on both Figs.

4 and 7 were examined. Figure 8 shows normalized DSDs as well as Fig. 4. A shape of the distributions is quite similar to the all data (Fig. 4a), but significantly different in the number concentrations between 1.5 mm and 3.0 mm in diameter, and the percentile ranges are narrower in Fig. 8 than in Fig. 4a. In addition, the distributions are like an exponential distribution except lower concentrations in smaller (<0.5 mm) diameter, which means that nearly the same distribution could be assumed in terms of exponential distribution. The K_{DP}–R relation for stronger R will be discussed in the following subsection.

Fig. 8

4.2 Toward improvement of QPE in Japan

Previous studies have shown that the coefficient *a* and exponent *b* of the K_{DP}–R relation vary regionally (Table 2). The coefficients obtained from C-band polarimetric radar and/or ground-based observations at different locations showed that the value of coefficient *a* (25.1) at Kumagaya was close to values in the UK (24.7) and Okinawa, Japan (28.8), whereas the value of exponent *b* at Kumagaya was close to values in Tropics (0.78) and Taiwan (0.80). In contrast, the value of the coefficient *a* at Tokyo (30.9) was larger than its value at Kumagaya (25.1), probably due to the vertical variabilities of radar reflectivity (Zawadzki 1984; Austin 1987; Kitchen and Jackson 1993; Anagnostou and Krajewski 1999; Villarini and Krajewski 2010). For example, the Japan Meteorological Agency uses ground-based observations (i.e., rain gauge data) to adjust R values obtained from weather radar observations at an altitude of roughly 2 km (Nagata 2011), even if R changes in the vertical direction. However, vertical differences in R need to be considered when weather radar is

Table 2

being used to capture conditions before heavy rainfall is observed at ground level, and they are also important for capturing precursors to heavy rainfall. An investigation of this point was outside the scope of this study but remains for future work.

The results of this study suggested that the K_{DP}–R relation used in Yamauchi et al. (2012) and Adachi et al. (2015) for C-band polarimetric weather radar observations could be improved for strong rainfall events by considering the condition with $\Lambda < 2$ mm^{-1} because their studies were based on one event and did not examine the K_{DP}–R relation directory using in situ observational data. Yamauchi et al. (2012) showed that the estimated R using the K_{DP}–R relation proposed by Bringi and Chandrasekar (2001) was in good agreement with the R obtained from an optical disdrometer for only one heavy rainfall event occurred in August. The K_{DP}–R relation used in their study is based on weather radar related coefficients (i.e., not near the ground but above a few km), which may cause a little higher value of coefficient a as shown in Table 2. Adachi et al. (2015) also used the same K_{DP}–R relation and compared R for only one event that occurred in December. As described in the previous subsection, the K_{DP}–R relation for stronger R was examined. The obtained coefficients were quite similar to the annual mean value, but the value of a is a little larger in the cases of stronger R cases than in the annual mean. These coefficients were probably optimized for heavy rainfall events because nearly the same size distribution in terms of the slope parameter was obtained (Fig. 8 and Table 1). Consequently, the slope parameters obtained in this study could be used to optimize the K_{DP}–R relation, which has been specifically improved for Japan, to make a QPE method suitable for heavy rainfall in operational use.

5. Summary and Conclusions

The characteristics of DSDs were statistically clarified by using about 10 years of DSD data obtained in Kumagaya, eastern Japan. The results showed that DSDs tended to be distributed in a specific area, i.e., D_m ~2.0–3.0 mm and N_w ~2×10^3–3×10^4 mm^{-1} m^{-3}, in the DSD parameter (D_m–N_w) space when R is stronger (>=40 mm hr^{-1}). For the quasi-equilibrium DSDs, the contribution of temporal changes in both N_w and D_m to increments of R was found to be large whereas the contribution to R was large when D_m or N_w was effectively increased with temporal change based on an error analysis.

In terms of QPE, the coefficient and exponent of the K_{DP}–R relation, which had previously been calculated on a case-by-case basis, were statistically evaluated to identify characteristics that depended on seasonality and DSD variation. The results showed that the coefficient in the K_{DP}–R relation tended to be larger in the warm season (from May to October) and smaller in the cold season (from January to April and from November to December) when assuming the fixed temperature of 10 degrees Celsius, whereas the exponent of the relation had no apparent trend. It is likely, however, that the K_{DP}–R relation could be optimized for heavy rainfall events in Japan by using the slope parameter.

The present results should be statistically evaluated by using two-dimensional (geospatial) distributions or three-dimensional (geospatial and vertical) information of the three-dimensional structures of precipitating systems, obtained from polarimetric weather radar observations. The present results, which provided a basis for such a statistical evaluation for the first time, are expected to be very useful in this regard. An evaluation using polarimetric weather radar observations, i.e., vertical variations of DSDs in terms of process-oriented perspective, was outside the scope of this study and remains for future work. To improve understanding of the characteristics of DSDs and cloud microphysical processes based on observational facts, analyses such as the present study should be conducted in multiple regions in different climatic zones.

Data Availability Statement

The research data and code used in this study are available from the corresponding author on request.

Acknowledgments

The authors wish to express their gratitude to the two anonymous reviewers and the editor in charge for their valuable feedback and suggestions, which have led to significant improvements in the original manuscript. Constructive comments from Dr. Takahisa Kobayashi (Meteorological Research Institute; MRI) and Dr. Kazuhiko Masuda (MRI) at the early stage of this study about interpreting DSD data improved the quality of this manuscript and are especially acknowledged. The first author also thanks Dr. Hideaki Mouri (MRI) for lending him the book by Bevington and Robinson (2003), which was consulted for the derivations of Eqs. (9) and (10) and for creating Fig. 6 in this study. This work was financially supported by the Japan Society for the Promotion of Science (JSPS) Grant-in-Aid for Early Career Scientists (Grant Number JP24K17126). The sixth author was supported in part by JSPS Grant-in-Aid for Scientific Research (C) (Grant Number JP20K04092).

Appendix

To compare the slope of size distribution, the stationary distributions and the exponential distributions are shown in Fig. A1. For the stationary distribution obtained in McFarquhar (2004a) and Straub et al. (2010), the tail slopes of these distributions are approaching $\Lambda = 2.0\ \mathrm{mm}^{-1}$. In contrast, the slopes in the smaller (<1.6 mm) diameter range are larger than $\Lambda = 2.0\ \mathrm{mm}^{-1}$.

References

Adachi, A., T. Kobayashi, and H. Yamauchi, 2015: Estimation of raindrop size distribution and rainfall rate from polarimetric radar measurements at attenuating frequency based on the self-consistency principle. *J. Meteor. Soc. Japan*, **93**, 359–388, doi:10.2151/jmsj.2015-020.

Adachi, A., T. Kobayashi, H. Yamauchi, and S. Onogi, 2013: Detection of potentially hazardous convective clouds with a dual-polarized C-band radar. *Atmos. Meas. Tech.*, **6**, 2741–2760, doi:10.5194/amt-6-2741-2013.

Anagnostou, E. N., and W. F. Krajewski, 1999: Real-time radar rainfall estimation. Part I: algorithm formulation. *J. Atmos. Oceanic Technol.*, 16, 189–197, doi:10.1175/1520-0426(1999)016<0189:RTRREP>2.0.CO;2.

Asselin de Beauville, C., R. H. Petit, G. Marion, and J. P. Lacaux, 1988: Evolution of peaks in the spectral distribution of raindrops from warm isolated maritime clouds. *J. Atmos. Sci.*, **45**, 3320–3332, doi:10.1175/1520-0469(1988)045<3320:EOPITS>2.0.CO;2.

Atlas, D., R. C. Srivastava, and R. S. Sekkon, 1973: Doppler radar characteristics of precipitation at vertical incidence. *Rev. Geophys.*, **2**, 1–35, doi:10.1029/RG011i001p00001.

Austin, P. M., 1987: Relation between measured radar reflectivity and surface rainfall. *Mon. Wea. Rev.*, 115, 1053–1070, doi:10.1175/1520-0493(1987)115<1053:RBMRRA>2.0.CO;2.

Beheng, K. D., K. Jellinghaus, W. Sander, W. Roth, and B. Weigand, 2006: Investigation of collision-induced breakup of raindrops by numerical simulations: First results. *Geophys. Res. Lett.*, **33**, L10811, doi:10.1029/2005GL025519.

Bevington, P. R., and D. K. Robinson, 2003: *Data reduction and error analysis for the physical sciences*. 3rd ed. McGraw-Hill higher education, 320 pp.

Bringi, V. N., and Chandrasekar V., 2001: *Polarimetric doppler weather radar*. Cambridge University Press, 636 pp.

Bringi, V. N., V. Chandrasekar, J. Hubbert, E. Gorgucci, W. L. Randeu, and M. Schönhuber, 2003: Raindrop size distribution in different climatic regimes from disdrometer and dual-polarized radar analysis. *J. Atmos. Sci.*, **60**, 354–365, doi:10.1175/1520-0469(2003)060<0354:RSDIDC>2.0.CO;2.

Bringi, V. N., M. Thurai, K. Nakagawa, G. J. Huang, T. Kobayashi, A. Adachi, H. Hanado, and S. Sekizawa, 2006: Rainfall estimation from C-band polarimetric radar in Okinawa, Japan: Comparisons with 2D-video disdrometer and 400 MHz wind profiler, 2006. *J. Meteor. Soc. Japan*, **84**, 705–724, doi:10.2151/jmsj.84.705.

Bringi, V. N., M. A. Rico-Ramirez, and M. Thurai, 2011: Rainfall estimation with an operational polarimetric C-band radar in the United Kingdom: Comparison with a gauge network and error analysis. *J. Hydrometeor.*, **12**, 935–954, doi:10.1175/JHM-D-10-05013.1.

Brown, P. S., 1986: Analysis of the Low and List drop-breakup formulation. *J. Appl. Meteor.*

Climatol., **25**, 313–321, doi:10.1175/1520-0450(1986)025<0313:AOTLAL>2.0.CO;2.

Brown, Jr., P. S., 1993: Analysis and parameterization of the combined coalescence, breakup, and evaporation processes. *J*. *Atmos*. *Sci*., **50**, 2940–2952, doi:10.1175/1520-0469(1993)050<2940:AAPOTC>2.0.CO;2

Chen, J., and D. Lamb, 1994: Simulation of cloud microphysical and chemical processes using a multicomponent framework. Part I: Description of the microphysical model. *J*. *Atmos*. *Sci*., **51**, 2613–2630, doi:10.1175/1520-0469(1994)051<2613:SOCMAC>2.0.CO;2.

Chen, G., K. Zhao, G. Zhang, H. Huang, S. Liu, L. Wen, Z. Yang, Z. Yang, L. Xu, and W. Zhu, 2017: Improving polarimetric C-band radar rainfall estimation with two-dimensional video disdrometer observations in eastern China. *J*. *Hydrometeor*., **18**, 1375–1391, doi:10.1175/JHM-D-16-0215.1.

D’Adderio, L. P., F. Porcù, and A. Tokay, 2015: Identification and analysis of collisional breakup in natural rain. *J*. *Atmos*. *Sci*., **72**, 3404–3416, doi:10.1175/JAS-D-14-0304.1.

D’Adderio, L. P., F. Porcù, and A. Tokay, 2018: Evolution of drop size distribution in natural rain. *Atmos*. *Res*., **200**, 70–76, doi:10.1016/j.atmosres.2017.10.003.

Dawson, D. T., E. R. Mansell, and M. R. Kumjian, 2015: Does wind shear cause hydrometeor size sorting?. *J*. *Atmos*. *Sci*., **72**, 340–348, doi:10.1175/JAS-D-14-0084.1.

Dolan, B., B. Fuchs, S. A. Rutledge, E. A. Barnes, and E. J. Thompson, 2018: Primary modes of global drop size distributions. *J*. *Atmos*. *Sci*., **75**, 1453–1476, doi:10.1175/JAS-

D-17-0242.1.

Feingold, G., S. Tzivion (Tzitzvashvili), and Z. Leviv, 1988: Evolution of raindrop spectra. Part I: Solution to the stochastic collection/breakup equation using the method of moments. *J. Atmos. Sci.*, **45**, 3387–3399, doi:10.1175/1520-0469(1988)045<3387:EORSPI>2.0.CO;2.

Figueras i Ventura, J., A.-A. Baumahmoud, B. Fradon, P. Dupuy, and P. Tabary, 2012: Long-term monitoring of French polarimetric radar data quality and evaluation of several polarimetric quantitative precipitation estimators in ideal conditions for operational implementation at C-band. *Quart. J. Roy. Meteor. Soc.*, **138**, 2212–2228, doi:10.1002/qj.1934.

Friedrich, K., E. A. Kalina, F. J. Masters, and C. R. Lopez, 2013: Drop-size distributions in thunderstorms measured by optical disdrometers during VORTEX2. *Mon. Wea. Rev.*, **141**, 1182–1203, doi:10.1175/MWR-D-12-00116.1.

Fritsch, J. M., and R. E. Carbone, 2004: Improving quantitative precipitation forecasts in the warm season: A USWRP research and development strategy. *Bull. Amer. Meteor. Soc.*, **85**, 955–966, doi:10.1175/BAMS-85-7-955.

Garcia-Garcia, F., and J. E. Gonzalez, 2000: Raindrop spectra observations from convective showers in the valley of Mexico. *Proc. 13th Int. Conf. on Clouds and Precipitation*, Reno, NV, 398–401.

Hardin, J., and N. Guy, 2017: PyDisdrometer v1.0, *Zenodo*, doi:10.5281/zenodo.9991.

Hirockawa, Y., T. Kato, K. Araki, and W. Mashiko, 2020: Characteristics of an extreme rainfall event in Kyushu district, southwestern Japan in early July 2020. *SOLA*, **16**, 265–270, doi:10.2151/sola.2020-044.

Hu, Z., and R. C. Srivastava, 1995: Evolution of raindrop size distribution by coalescence, breakup, and evaporation: Theory and observations, *J. Atmos. Sci.*, **52**, 1761–1783, doi:10.1175/1520-0469(1995)052<1761:EORSDB>2.0.CO;2.

Kato, T., 2020: Quasi-stationary band-shaped precipitation systems, named “senjo-kousuitai”, causing localized heavy rainfall in Japan. *J. Meteor. Soc. Japan*, **98**, 485–509, doi:10.2151/jmsj.2020-029.

Keenan, T. D., L. D. Carey, D. S. Zrnić, and P. T. May, 2001: Sensitivity of 5-cm wavelength polarimetric radar variables to raindrop axial ratio and drop size distribution. *J. Appl. Meteor. Climatol.*, **40**, 526–545, doi:10.1175/1520-0450(2001)040<0526:SOCWPR>2.0.CO;2.

Kitchen, M., and P. M. Jackson, 1993: Weather radar performance at long range–simulated and observed. *J. Appl. Meteor. Climatol.*, **32**, 975–985, doi:10.1175/1520-0450(1993)032<0975:WRPALR>2.0.CO;2.

Kollias, P., B. A. Albrecht, and F. D. Marks Jr., 2001: Raindrop sorting induced by vertical drafts in convective clouds. *Geophys. Res. Lett.*, **28**, 2787–2790, doi:10.1029/2001GL013131.

List, R., N. R. Donaldson, and R. E. Stewart, 1987: Temporal evolution of drop spectra to collisional equilibrium in steady and pulsating rain. *J. Atmos. Sci.*, **44**, 362–372, doi:10.1175/1520-0469(1987)044<0362:TEODST>2.0.CO;2.

Löffler-Mang, M., and J. Joss, 2000: An optical disdrometer for measuring size and velocity of hydrometeors. *J. Atmos. Oceanic Technol.*, **17**, 130–139, doi:10.1175/1520-0426(2000)017<0130:AODFMS>2.0.CO;2.

Low, T. B., and R. List, 1982: Collision, coalescence and breakup of raindrops. Part I: Experimentally established coalescence efficiencies and fragment size distributions in breakup. *J. Atmos. Sci.*, **39**, 1591–1606, doi:10.1175/1520-0469(1982)039<1591:CCABOR>2.0.CO;2.

May, P. T., T. D. Keenan, D. S. Zrnić, L. D. Carey, and S. A. Rutledge, 1999: Polarimetric radar measurements of tropical rain at a 5-cm wavelength. *J. Appl. Meteor. Climatol.*, **38**, 750–765, doi:10.1175/1520-0450(1999)038<0750:PRMOTR>2.0.CO;2.

McFarquhar, G. M., 2004a: A new representation of collision-induced breakup of raindrops and its implications for the shapes of raindrop size distributions. *J. Atmos. Sci.*, **61**, 777–794, doi:10.1175/1520-0469(2004)061<0777:ANROCB>2.0.CO;2.

McFarquhar, G. M., 2004b: The effect of raindrop clustering on collision-induced break-up of raindrops. *Quart. J. Roy. Meteor. Soc.*, **130**, 2169–2190, doi:10.1256/qj.03.98.

McFarquhar, G. M., 2010: Raindrop size distribution and evolution. *Rainfall: State of the Science*, *Geophys. Monogr.*, **191**, Amer. Geophys. Union, 49–60, doi:10.1029/2010GM000971.

McFarquhar, G. M., R. List, 1991: The evolution of three-peak raindrop size distributions in one-dimensional shaft models. Part II: multiple pulse rain. *J. Atmos. Sci.* **48**, 1587–1595, doi:10.1175/1520-0469(1991)048<1587:TEOTPR>2.0.CO;2.

McFarquhar, G. M., and R. List, 1993: The effect of curve fits for the disdrometer calibration on raindrop spectra, rainfall rate, and radar reflectivity. *J. Appl. Meteor. Climatol.*, **32**, 774–782, doi:10.1175/1520-0450(1993)032<0774:TEOCFF>2.0.CO;2.

McFarquhar, G. M., R. List, D. R. Hudak, R. P. Nissen, J. S. Dobbie, N. P. Tung, and T. S. Kang, 1996: Flux measurements of pulsating rain with a disdrometer and Doppler radar during phase II of the Joint Tropical Rain Experiment in Malaysia. *J. Appl. Meteor. Climatol.*, **35**, 859–874, doi:10.1175/1520-0450(1996)035<0859:FMOPRW>2.0.CO;2.

Mishchenko, M. I., L. D. Travis, and D. W. Mackowski, 1996: T-matrix computations of light scattering by nonspherical particles: A review. *J. Quant. Spectrosc. Radiat. Transfer*, **55**, 535–575, doi:10.1016/0022-4073(96)00002-7.

Misumi R, Y. Uji, and T. Maesaka 2021: Modification of raindrop size distribution due to seeder–feeder interactions between stratiform precipitation and shallow convection observed by X-band polarimetric radar and optical disdrometer. *Atmos. Sci. Lett.*, **22**, e1034, doi:10.1002/asl.1034.

Murata, F., T. Terao, K. Chakravarty, H. J. Syiemlieh, and L. Cajee, 2020: Characteristics of orographic rain drop-size distribution at Cherrapunji, northeast India. *Atmosphere*, **11**, 777, doi:10.3390/atmos11080777.

Nagata, K., 2011: Quantitative precipitation estimation and quantitative precipitation forecasting by the Japan Meteorological Agency. *RSMC Tokyo–Typhoon Center Technical Review*, **13**, 37-50. [Available online at: http://www.jma.go.jp/jma/jma-eng/jma-center/rsmc-hp-pub-eg/techrev/text13-2.pdf, accessed 25 January 2024.]

Otsubo, A., and A. Adachi, 2024: Short-term predictability of extreme rainfall using dual-polarization radar measurements. *J. Meteor. Soc. Japan*, **102**, 151–165, doi:10.2151/jmsj.2024-007.

Prat, O. P., and A. P. Barros, 2007: A robust numerical solution of the stochastic collection–breakup equation for warm rain. *J. Appl. Meteor. Climatol.*, **46**, 1480–1497, doi:10.1175/JAM2544.1.

Ryzhkov, A. V., and D. S. Zrnić, 1998: Discrimination between rain and snow with a polarimetric radar. *J. Appl. Meteor. Climatol.*, **37**, 1228–1240, doi:10.1175/1520-0450(1998)037<1228:DBRASW>2.0.CO;2.

Ryzhkov, A. V., and D. S. Zrnić, 2019: *Radar Polarimetry for Weather Observations*. Springer, 497 pp.

Sachidananda, M., and D. S. Zrnić, 1987: Rain rate estimates from differential polarization measurements. *J. Atmos. Oceanic Technol.*, **4**, 588–598, doi:10.1175/1520-0426(1987)004<0588:RREFDP>2.0.CO;2.

Scarchilli, G., E. Gorgucci, V. Chandrasekar, and T. A. Seliga, 1993: Rainfall estimation using polarimetric techniques at C-band frequencies. *J. Appl. Meteor. Climatol.*, **32**, 1150–1160, doi:10.1175/1520-0450(1993)032<1150:REUPTA>2.0.CO;2.

Schlottke, J., W. Straub, K. D. Beheng, H. Gomaa, and B. Weigand, 2010: Numerical investigation of collision-induced breakup of raindrops. Part I: Methodology and dependencies on collision energy and eccentricity. *J. Atmos. Sci.*, **67**, 557–575, doi:10.1175/2009JAS3174.1.

Sheppard, B. E. 1990: Effect of irregularities in the diameter classification of raindrops by the Joss-Waldvogel disdrometer. *J. Atmos. Oceanic Technol.*, **7**, 180–183, doi:10.1175/1520-0426(1990)007<0180:EOIITD>2.0.CO;2.

Steiner, M., and A. Waldvogel, 1987: Peaks in raindrop size distributions. *J. Atmos. Sci.*, **44**, 3127–3133, doi:10.1175/1520-0469(1987)044<3127:PIRSD>2.0.CO;2.

Straub, W., K. D. Beheng, A. Seifert, J. Schlottke, and B. Weigand, 2010: Numerical investigation of collision-induced breakup of raindrops. Part II: Parameterizations of coalescence efficiencies and fragment size distributions. *J. Atmos. Sci.*, **67**, 576–588, doi:10.1175/2009JAS3175.1.

Testud, J., S. Oury, R. A. Black, P. Amayenc, and X. Dou, 2001: The concept of “Normalized” distribution to describe raindrop spectra: A tool for cloud physics and cloud remote sensing. *J. Appl. Meteor. Climatol.*, **40**, 1118–1140, doi:10.1175/1520-0450(2001)040<1118:TCONDT>2.0.CO;2.

Thompson, E. J., S. A. Rutledge, B. Dolan, M. Thurai, and V. Chandrasekar, 2018: Dual-polarization radar rainfall estimation over tropical oceans. *J. Appl. Meteor. Climatol.*, **57**, 755–775, doi:10.1175/JAMC-D-17-0160.1.

Tokay, A., W. A. Petersen, P. Gatlin, and M. Wingo, 2013: Comparison of raindrop size distribution measurements by collocated disdrometers. *J. Atmos. Oceanic Technol.*, **30**, 1672–1690, doi:10.1175/JTECH-D-12-00163.1.

Tokay, A., D. B. Wolff, and W. A. Petersen, 2014: Evaluation of the new version of the laser-optical disdrometer, OTT Parsivel^2. *J. Atmos. Oceanic Technol.*, **31**, 1276–1288, doi:10.1175/JTECH-D-13-00174.1.

Tsuguti, H., and T. Kato, 2014: Objective extraction of heavy rainfall events and statistical analysis on their characteristic features. *Tenki*, **61**, 455–469. (in Japanese)

Unuma, T., 2024: Three-dimensional structure of an equilibrium drop size distribution within a convective system in Japan. *SOLA*, **20**, 47−54, doi:10.2151/sola.2024-007.

Unuma, T., and T. Takemi, 2016: Characteristics and environmental conditions of quasi-stationary convective clusters during the warm season in Japan. *Quart. J. Royal Meteor. Soc.*, **142**, 1232–1249, doi:10.1002/qj.2726.

Unuma, T., and T. Takemi, 2021: Rainfall characteristics and their environmental conditions during the heavy rainfall events over Japan in July of 2017 and 2018. *J. Meteor. Soc. Japan*, **99**, 165–180, doi:10.2151/jmsj.2021-009.

Unuma, T., H. Yamauchi, A. Umehara, and T. Kato, 2023: An equilibrium raindrop size distribution associated with a heavy-rain-producing convective system in Japan. *SOLA*, **19**, 150–156, doi:10.2151/sola.2023-020.

Valdez, M. P., and K. C. Young, 1985: Number fluxes in equilibrium raindrop populations: A Markov chain analysis. *J. Atmos. Sci.*, **42**, 1024–1036, doi:10.1175/1520-0469(1985)042<1024:NFIERP>2.0.CO;2.

Villarini, G., and W. F., Krajewski, 2010: Review of the different sources of uncertainty in single polarization radar-based estimates of rainfall. *Surv. Geophys*, 31, 107–129, doi:10.1007/s10712-009-9079-x.

Vulpiani, G., M. Montopoli, L. D. Passeri, A. G. Gioia, P. Giordano, and F. S. Marzano, 2012: On the use of dual-polarized C-band radar for operational rainfall retrieval in mountainous areas. *J. Appl. Meteor. Climatol.*, **51**, 405–425, doi:10.1175/JAMC-D-10-05024.1.

Wang, Y., J. Zhang, A. V. Ryzhkov, and L. Tang, 2013: C-band polarimetric radar QPE based on specific differential propagation phase for extreme typhoon rainfall. *J. Atmos. Oceanic Technol.*, **30**, 1354–1370, doi:10.1175/JTECH-D-12-00083.1.

Willis, P. T., and P. Tattelman, 1989: Drop-size distributions associated with intense rainfall. *J. Appl. Meteor. Climatol.*, **28**, 3–15, doi:10.1175/1520-0450(1989)028<0003:DSDAWI>2.0.CO;2.

WMO, 2024: The Guide to Operational Weather Radar Best Practices (WMO-No.1257) Volume VI: *Weather Radar Data and Processing*. [Available online at: https://community.wmo.int/en/activity-areas/imop/new-provisional-2024-edition-guide-operational-weather-radar-best-practices, accessed 17 April 2024.]

Yamauchi, H., A. Adachi, O. Suzuki, and T. Kobayashi, 2012: Precipitation estimate of a heavy rain event using a C-band solid-state polarimetric radar. *7th European Conference on Radar in Meteorology and Hydrology*, Toulouse, France, 201 SP.

Zawadzki, I., 1984: Factors affecting the precision of radar measurements of rain. Preprints, *22nd Conference on Radar Meteorology*, Zurich, Switzerland, Amer. Meteor. Soc., 251–256.

Zawadzki, I., and M. De Agostinho Antonio, 1988: Equilibrium raindrop size distributions in tropical rain. *J. Atmos. Sci.*, **45**, 3452–3459, doi:10.1175/1520-0469(1988)045<3452:ERSDIT>2.0.CO;2.

Zhang, G., M. Xue, Q. Cao, and D. Dawson, 2008: Diagnosing the intercept parameter for exponential raindrop size distribution based on video disdrometer observations: Model development. *J. Appl. Meteor. Climatol.*, **47**, 2983–2992, doi:10.1175/2008JAMC1876.1.

Zrnić, D. S., and A. Ryzhkov, 1996: Advantages of rain measurements using specific differential phase. *J. Atmos. Oceanic Technol.*, **13**, 454–464, doi:10.1175/1520-0426(1996)013<0454:AORMUS>2.0.CO;2.

List of Figures

Fig. 1 Location of the in situ precipitation measurement site in Kumagaya, Japan (cross), where both a first-generation OTT-Parsivel disdrometer (upper left) and a tipping-bucket-type rain gauge are installed at the Kumagaya Local Meteorological Office, Japan Meteorological Agency.

Fig. 2 Scatter plot of the first-generation OTT-Parsivel data versus tipping-bucket-type rain gauge data in relation to the 1-min rainfall intensity (mm hr^{-1}) (color scale). The equation of the line fitted to the data (blue line) and the correlation coefficient between the two datasets are displayed in the upper left.

Fig. 3 Scatter plot of the mass-weighted mean diameter (D_m; mm) versus the generalized intercept parameter (N_w; mm^{-1} m^{-3}) in 1-min drop size distribution observations in relation to rainfall intensity (R; mm hr^{-1}) (color scale). Regions in the two-dimensional space of continental convection (solid line rectangle), maritime convection (dashed line rectangle), and stratiform conditions (dotted line), as classified by Bringi et al. (2003), are also shown. The markers of star, square, cross, and triangle represents the data of the first, second, third, and fourth quadrants categorized in Fig. 6, respectively.

Fig. 4 Drop size distributions ($N(D)$; mm^{-1} m^{-3}) normalized by the total number concentrations during each 1-min period (N_t; m^{-3}): (a) all 1-min data, and (b) 1-min data with highest slope (HS; mm^{-2} m^{-3}) > 0 and coefficient of determination regression score of the two stationary distributions (McFarquhar 2004a or Straub et al. 2010) equal to or larger than 0.9. The reference distributions obtained by McFarquhar (2004a), and Straub et al. (2010) are also shown. The black solid lines show median values, the gray dashed lines show the 25th and 75th percentile values, and the gray dotted lines show the 10th and 90th percentile values.

Fig. 5 Frequency distribution of equivalent volume diameter (D_e; mm) at inflection point occurred corresponding to the detected quasi-equilibrium drop size distributions. The D_e categories are 1.05, 1.17, 1.35, and 1.59.

Fig. 6 Scatter plot between the two terms on the right-hand side of Eq. (10) in relation to differences of rainfall intensity (R) between the time when a quasi-equilibrium drop size distributions was detected, and 1 min earlier (color scale). The data of the first, second, third, and fourth quadrants were categorized with the markers of star, square, cross, and triangle, respectively, as well as Fig. 3.

Fig. 7 Scatter plot of slope parameter (Λ; mm^{-1}) versus rainfall intensity (R; mm hr^{-1}) in relation to the two-dimensional frequency of occurrence (color scale). The crosses indicate the detected quasi-equilibrium drop size distribution cases.

Fig. 8 The same as Fig. 4, but for rainfall intensity R >= 40 mm hr^{-1} and the slope parameter $\Lambda < 2$ mm^{-1}.

Fig. A1 The stationary distributions for McFarquhar (2004a) (blue) and Straub et al. (2010) (orange). To compare the slope parameter of the exponential distribution with the stationary distributions, $N(D) = 4 \times 10^4 \exp(-\Lambda D)$ with $\Lambda = 2.0$ mm^{-1} (black dash) and 1.0 mm^{-1} (black dot) are displayed as a reference.

List of Tables

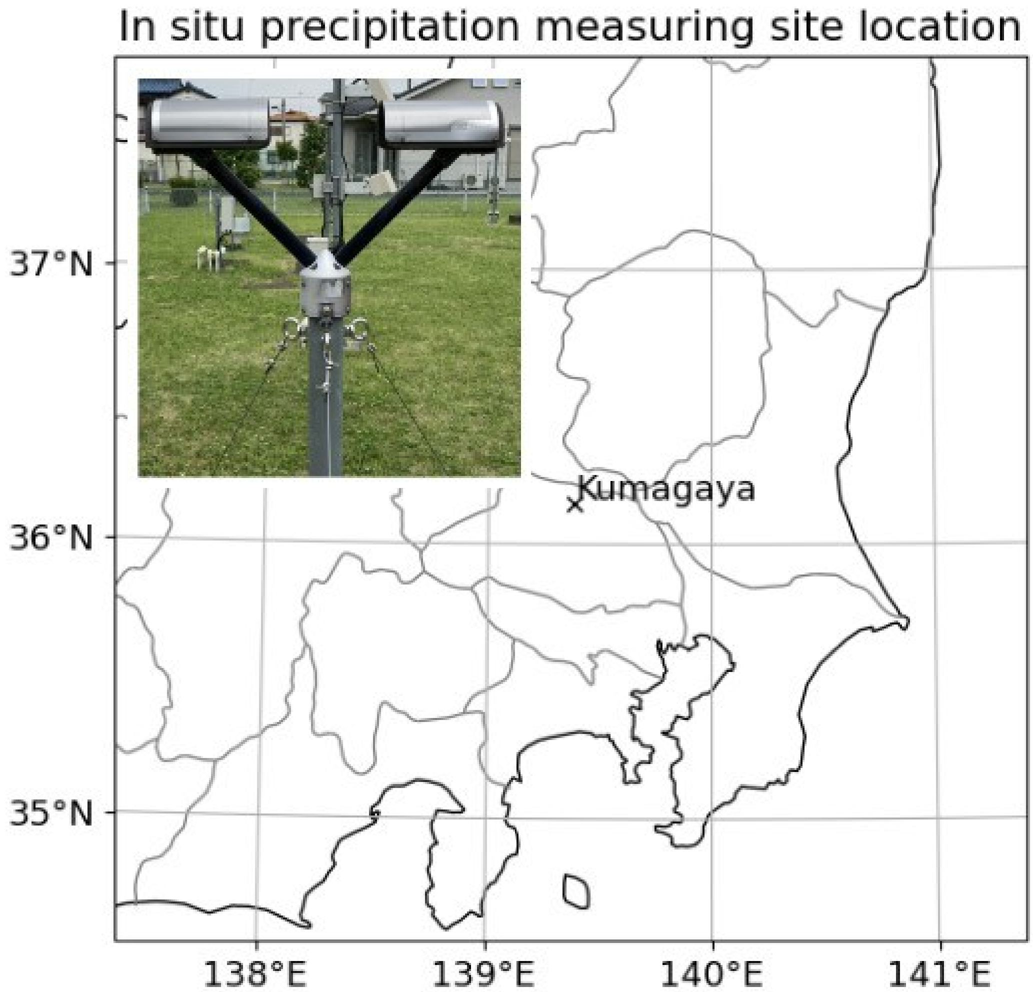

Fig. 1. Location of the in situ precipitation measurement site in Kumagaya, Japan (cross), where both a first-generation OTT-Parsivel disdrometer (upper left) and a tipping-bucket-type rain gauge are installed at the Kumagaya Local Meteorological Office, Japan Meteorological Agency.

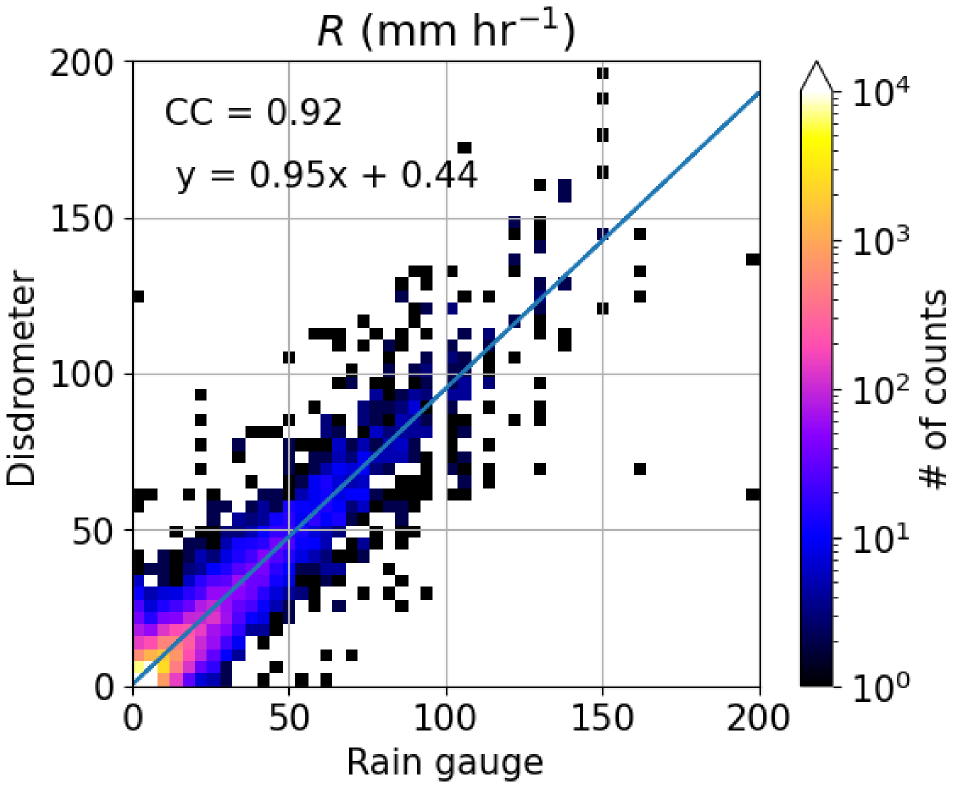

Fig. 2. Scatter plot of the first-generation OTT-Parsivel data versus tipping-bucket-type rain gauge data in relation to the 1-minute rainfall intensity (mm hr^{-1}) (color scale). The equation of the line fitted to the data (blue line) and the correlation coefficient between the two datasets are displayed in the upper left.

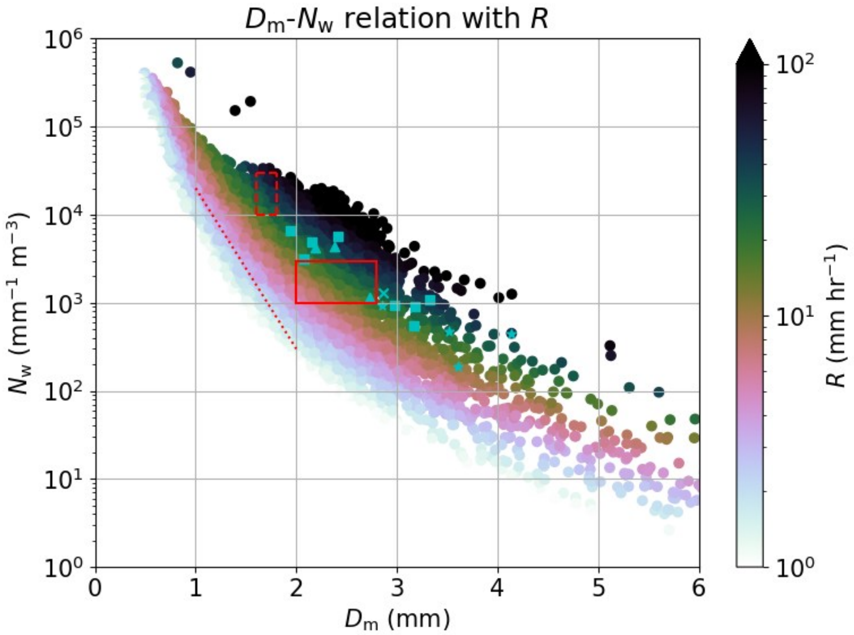

Fig. 3. Scatter plot of the mass-weighted mean diameter (D_m; mm) versus the generalized intercept parameter (N_w; mm^{-1} m^{-3}) in 1-min drop size distribution observations in relation to rainfall intensity (R; mm hr^{-1}) (color scale). Regions in the two-dimensional space of continental convection (solid line rectangle), maritime convection (dashed line rectangle), and stratiform conditions (dotted line), as classified by Bringi et al. (2003), are also shown. The markers of star, square, cross, and triangle represents the data of the first, second, third, and fourth quadrants categorized in Fig. 6, respectively.

(a)

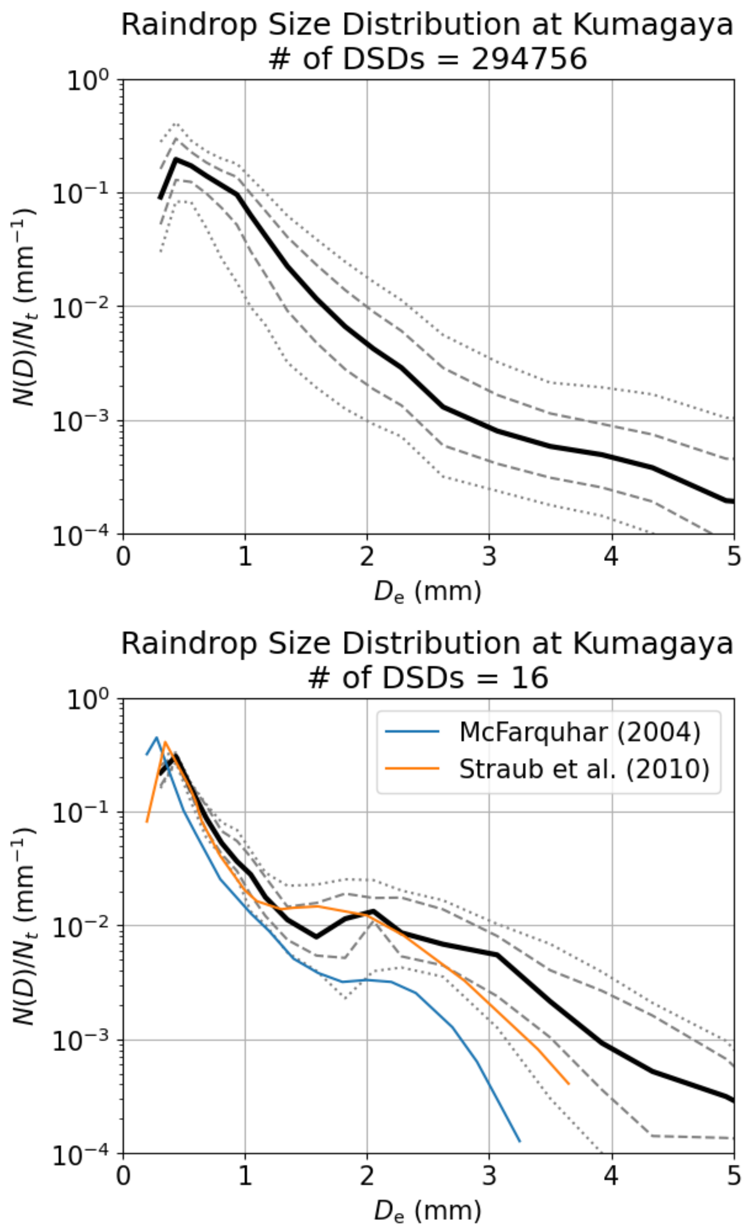

Fig. 4. Drop size distributions ($N(D)$; mm^{-1} m^{-3}) normalized by the total number concentrations during each 1-min period (N_t; m^{-3}): (a) all 1-min data, and (b) 1-min data with highest slope (HS; mm^{-2} m^{-3}) > 0 and coefficient of determination regression score of the two stationary distributions (McFarquhar 2004a or Straub et al. 2010) equal to or larger than 0.9. The reference distributions obtained by McFarquhar (2004a), and Straub et al. (2010) are also shown. The black solid lines show median values, the gray dashed lines show the 25th and 75th percentile values, and the gray dotted lines show the 10th and 90th percentile values.

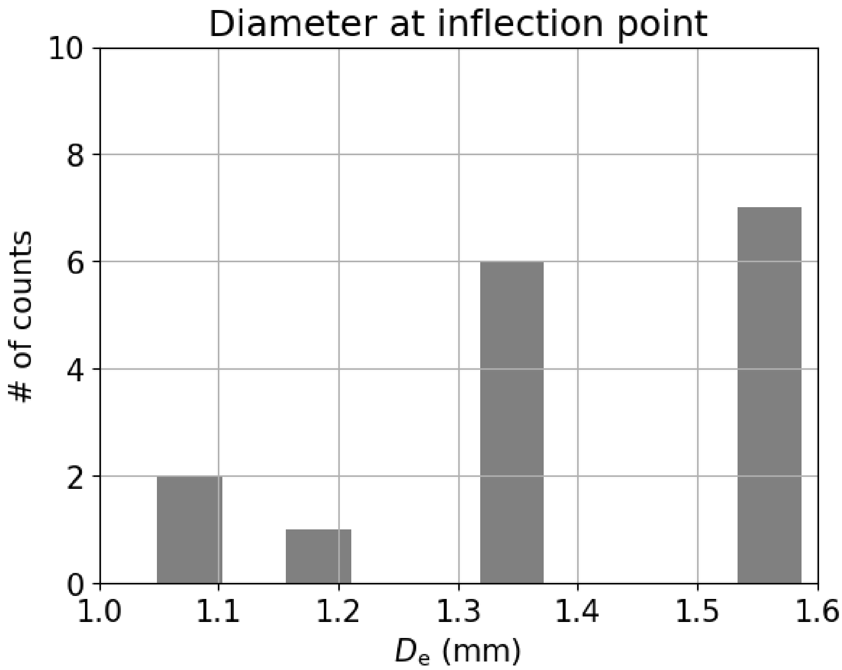

Fig. 5. Frequency distribution of equivalent volume diameter (D_e; mm) at inflection point occurred corresponding to the quasi-equilibrium drop size distributions. The D_e categories are 1.05, 1.17, 1.35, and 1.59.

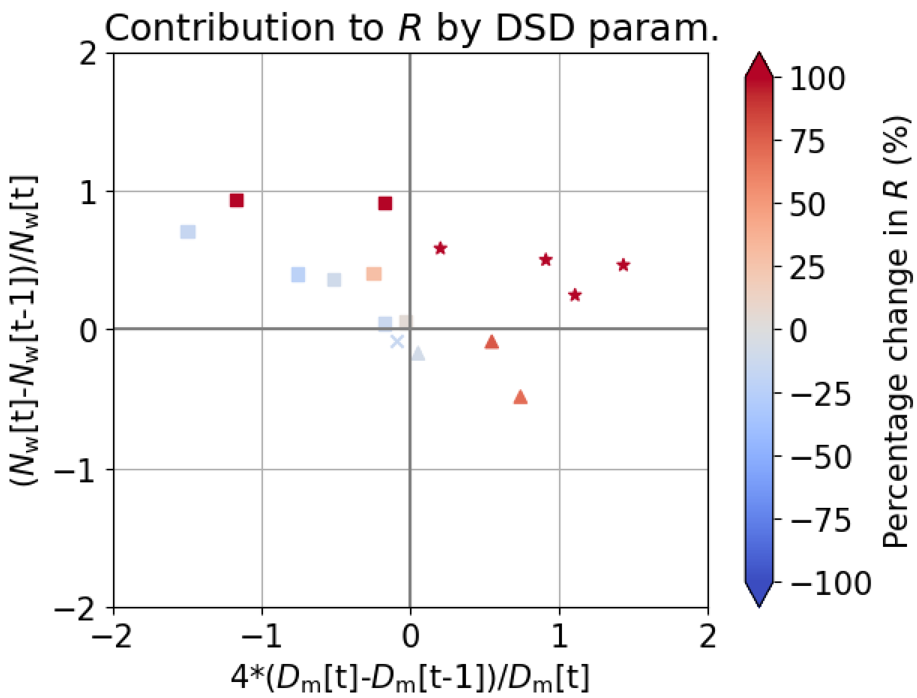

Fig. 6. Scatter plot between the two terms on the right-hand side of Eq. (10) in relation to differences of rainfall intensity (*R*) between the time when a quasi-equilibrium drop size distributions was detected, and 1 min earlier (color scale). The data of the first, second, third, and fourth quadrants were categorized with the markers of star, square, cross, and triangle, respectively, as well as Fig. 3.

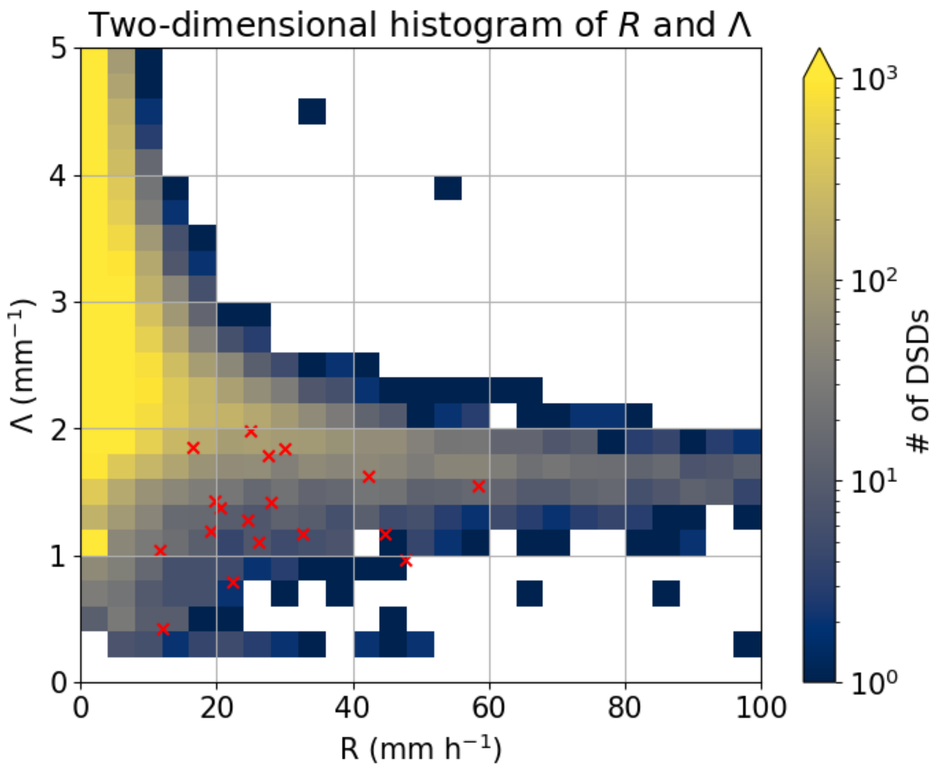

Fig. 7. Scatter plot of slope parameter (Λ; mm^{-1}) versus rainfall intensity (*R*; mm hr^{-1}) in relation to the two-dimensional frequency of occurrence (color scale). The crosses indicate the quasi-equilibrium drop size distribution cases.

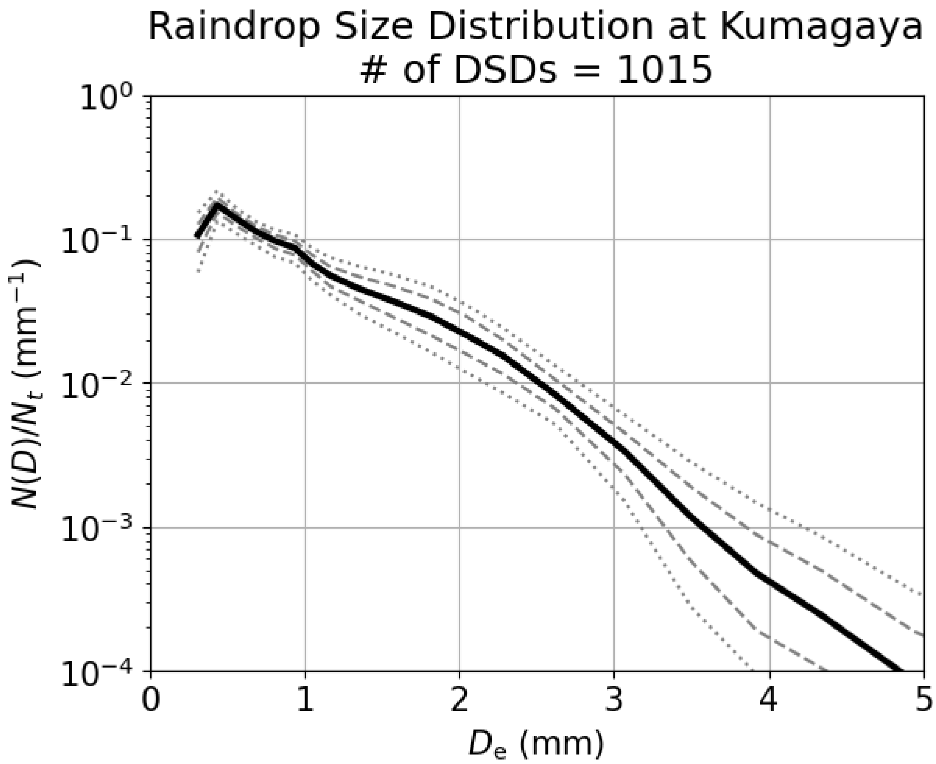

Fig. 8. The same as Fig. 4, but for rainfall intensity R >= 40 mm hr^{-1} and the slope parameter $\Lambda < 2$ mm^{-1}.

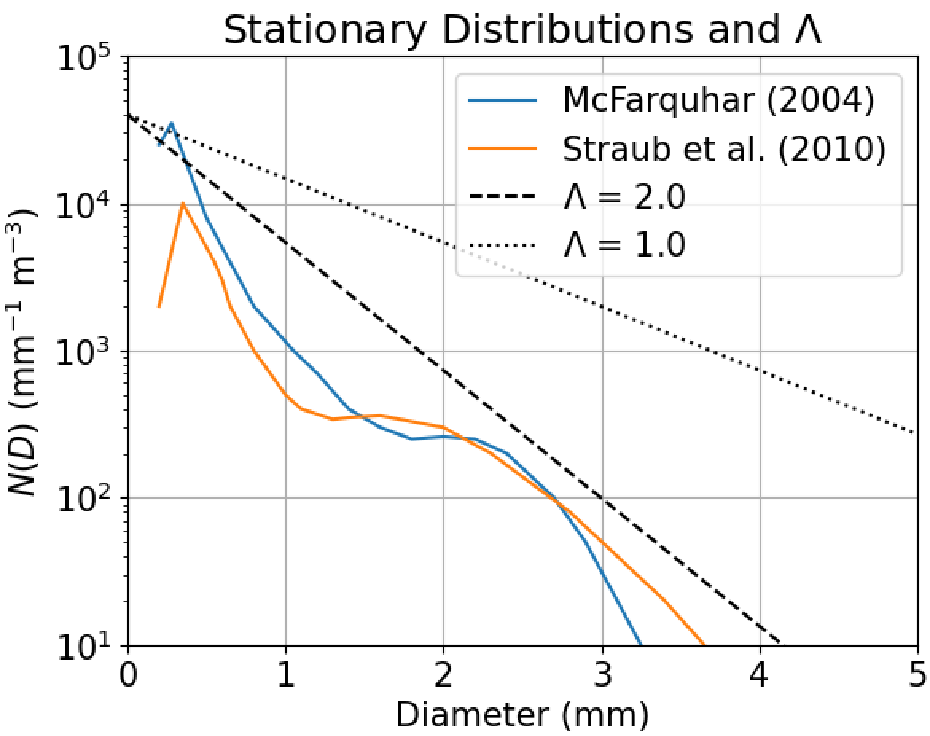

Fig. A1. The stationary distributions for McFarquhar (2004a) (blue) and Straub et al. (2010) (orange). To compare the slope parameter of the exponential distribution with the stationary distributions, $N(D) = 4\times10^4 \exp(-\Lambda D)$ with Λ = 2.0 mm^{-1} (black dash) and 1.0 mm^{-1} (black dot) are displayed as a reference.

Table 1: Coefficient *a* and exponent *b* of the K_{DP}–R relation (Eq. (11)) obtained from this study.

Month	***a***	***b***
January	14.9	0.69
February	19.7	0.78
March	20.0	0.75
April	20.4	0.72
May	22.6	0.73
June	24.5	0.77
July	26.0	0.80
August	26.9	0.78
September	25.9	0.76
October	29.1	0.85
November	20.7	0.76
December	19.3	0.75
Annual mean	25.1	0.79
The cases for R >= 40 mm hr^{-1} and Λ < 2 mm^{-1}	27.7	0.74

Table 2: Values of coefficient *a* and exponent *b* obtained in various locations: Italy (Scarchilli et al. 1993; Vulpiani et al. 2012), Australia (May et al. 1999; Keenan et al. 2001), Japan (Yamauchi et al. 2012; This study), UK (Bringi et al. 2011), France (Figueras et al. 2012), Taiwan (Wang et al. 2013), and the tropics (Thompson et al. 2018). Also shown is the transmitting frequency of the radar *f* (GHz) used in each location. Note that, Yamauchi et al. (2012)'s coefficients are based on Bringi and Chandrasekar (2001).

a	***b***	***f***	**Reference**	**Place**
19.4	1.00	5.40	Scarchilli et al. (1993)	Italy
34.6	0.83	5.63	May et al. (1999)	Darwin, Australia
31.4	0.84	5.63	Keenan et al. (2001)	Darwin, Australia
28.8	0.85	5.34	Bringi et al. (2006)	Okinawa, Japan
24.7	0.81	5.60	Bringi et al. (2011)	UK
30.8	0.85	5.40	Vulpiani et al. (2012)	Italy
29.7	0.85	5.63	Figueras et al. (2012)	France
30.9	0.85	5.37	Yamauchi et al. (2012)	Tokyo, Japan
35.4	0.80	5.60	Wang et al. (2013)	Taiwan
30.6	0.78	5.45	Thompson et al. (2018)	Tropics
25.1	0.79	5.40	This study	Kumagaya, Japan